CZECH TECHNICAL UNIVERSITY
IN PRAGUE

Faculty of Nuclear Sciences and Physical
Engineering
Department of Physics

Research project

Upsilon meson analysis at the STAR experiment

Bc. Oliver Matonoha

Supervisor: Ing. Olga Rusňáková, PhD.

Prague, 2017

ČESKÉ VYSOKÉ UČENÍ TECHNICKÉ
V PRAZE
Fakulta jaderná a fyzikálně inženýrská
Katedra fyziky

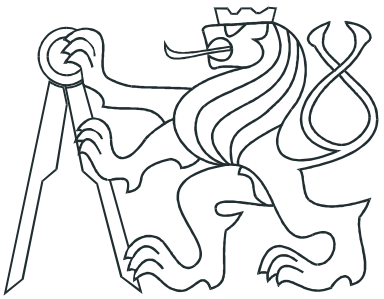

Výzkumný úkol

Analýza mesonu Upsilon na experimentu STAR

Bc. Oliver Matonoha

Školitel: Ing. Olga Rusňáková, PhD.

Praha, 2017

Prohlášení:

Prohlašuji, že jsem svůj výzkumný úkol vypracoval samostatně a použil jsem pouze podklady (literaturu, projekty, software, atd.) uvedené v přiloženém seznamu.

Nemám závažný důvod proti užití tohoto školního díla ve smyslu § 60 Zákona č. 121/2000 Sb., o právu autorském, o právech souvisejících s právem autorským a o změně některých zákonů (autorský zákon).

V Praze dne

Bc. Oliver Matonoha

Title:

Upsilon meson analysis at the STAR experiment

Author: Bc. Oliver Matonoha

Specialisation: Experimental nuclear and particle physics

Sort of project: Research project

Supervisor: Ing. Olga Rusňáková, PhD.

Abstract:

In ultra-relativistic heavy-ion collisions, creation of a novel state of matter is expected, in accordance with predictions by lattice QCD calculations. Under such extreme conditions, regular hadronic matter undergoes a phase transitions and forms a plasma of deconfined quarks and gluons (QGP). This medium is hypothesised to comprise the universe in its earliest stages. Researching the QGP properties can bring valuable input for early cosmological models as well as help us understand the character of the strong interaction.

Production of the quarkonium mesons is a crucial probe of the QGP, since its suppression can be viewed as a direct evidence of the plasma formation, due to the colour screening effect. Moreover, it can be used to infer constraints on the QGP temperature.

In this work, status of the author's analysis on Υ production at the STAR experiment in Au+Au collisions at $\sqrt{s_{\mathrm{NN}}} = 200$ GeV via the di-electron decay channel is reported. The reconstructed invariant mass spectra with extracted yields are presented. At RHIC energies, secondary effects complicating the measured suppression are deemed less significant for the Υ, which makes it a cleaner probe of the screening effect.

Key words: heavy-ion collisions, quark-gluon plasma, upsilon, quarkonium suppression, STAR

Název výzkumného úkolu:

Analýza mesonu Upsilon na experimentu STAR

Autor: Bc. Oliver Matonoha

Obor: Experimentální jaderná a částicová fyzika

Školitel: Ing. Olga Rusňáková, PhD.

Abstrakt:

Očekává se, že v ultra-relativistických srážkách těžkých iontů dochází k vytvoření nového stavu hmoty, dle předpovědí výpočtů QCD na mřížce. Za přítomných extrémních podmínek podstupuje běžná hadronová hmota fázový přechod a formuje plasma dekonfinovaných kvarků a gluonů (QGP). Je předpokládáno, že toto médium tvořilo vesmír v jeho nejranějších momentech. Zkoumání vlastností QGP může přinést cenné podněty pro kosmologické modely a vést k lepšímu pochopení charakteru silné interakce.

Produkce kvarkonií patří mezi zásadní sondy ke zkoumání QGP. Jejich potlačení lze chápat jako přímý důsledek vytvoření plasmatu kvůli barevnému stínění. Z měřené produkce lze rovněž vyvozovat limitní hodnoty teplot QGP.

V této práci autor představuje status své analýzy produkce mesonu Υ na experimentu STAR ve srážkách Au+Au při $\sqrt{s_{\mathrm{NN}}} = 200$ GeV za pomocí dvoj-elektronového rozpadového kanálu. Předneseny jsou rovněž zrekonstruovaná spektra invariantní hmoty s extrahovanými výtěžky. Sekundární vlivy ztěžující měřené potlačení produkce jsou pro Υ při energiích na RHICu považovány za méně významné. To činí z Υ jasnější sondy ke studování barevného stínění.

Klíčová slova: srážky těžkých iontů, quark-gluonové plasma, upsilon, potlačení kvarkonií, STAR

Acknowledgement

I would like to express my sincere gratitude to Dr. Rusňáková for her guidance over this analysis, her words of praise, and friendliness. Furthermore, I am also deeply grateful to Dr. Reed for her substantial and invaluable counsel. Finally, I would like to acknowledge my caring parents, without whose support my studies would not be possible in the first place.

Contents

List of Figures

Chapter 1

Introduction

This chapter serves as an introduction to the thesis. First, motivations behind and properties of heavy-ion collisions are briefly presented. In the second part, physics of heavy quarkonia are overviewed.

1.1 Heavy-ion collisions

Physics of heavy-ion collisions is a field of high energy physics studying collisions of massive atomic nuclei at ultra-relativistic energies. One of its principal motivations for this is the possible creation of the quark-gluon plasma (QGP) and its further analysis. Researching the QGP properties helps us understand the state of the universe in its earliest moments as well as the character of the strong interaction.

Heavy-ion collisions are studied at large particle accelerators—most notably RHIC and the LHC. Such collisions are *extreme* from various points of view. For instance, the hottest medium observed on Earth is created. The QGP is also found out to be the most vortical fluid, spinning up to 10^{22} per second. Its magnetic field is expected to be the strength of 10^{14} T, which is more than a thousandfold of the strongest magnetic field sources in the universe—the magnetars.

1.1.1 Collision kinematics and geometry

For the sake of conciseness, one uses *natural units* ($c, \hbar = 1$) in high energy physics problems. A heavy-ion collision is characterised by its centre-of-mass collision energy per nucleon pair $\sqrt{s_{\mathrm{NN}}}$. Particles coming from such collisions are then described with their Lorentz-invariant four-vectors $\mathbf{x} = (t, x, y, z)$, $\mathbf{p} = (E, p_x, p_y, p_z) = (E, p_{\mathrm{T}}, p_z)$. A following set of coordinates is also used for a laboratory frame centered around $x = y = z = 0$ (interaction point): φ (azimuthal angle), η (pseudorapidity), r (radius). The η is a function of polar angle θ—$\eta = -\log(\tan\frac{\theta}{2})$)—and, for high-momentum particles $p >> m$, can be related to rapidity $y = \frac{1}{2}\frac{E+p_z}{E-p_z}$. In these coordinates, following relations are valid:

$$p_x = |\vec{p_T}| \cos\varphi \ , \tag{1.1}$$

$$p_y = |\vec{p_T}| \sin\varphi \ , \tag{1.2}$$

$$p_z = |\vec{p}| \sinh\eta \ . \tag{1.3}$$

1.1.2 Event activity

Heavy-ion collisions are in essence collisions of two clusters of fluctuating nucleons and as such have many collision geometry configurations, which is an important factor for many processes. Impact parameter b is one of the variables used to describe said geometry. It is defined as the relative distance between the two nuclei centres in a plane transverse to the beam axis. Collisions with smaller b tend to have larger energy densities and temperatures.

Another important variable is the number of participants N_{part} and the number of binary nucleon collisions N_{coll}. The participants are those nucleons which actively participate in the collision, ie. have at least one interaction. Nucleons that are not participant are called the spectators. The N_{part} and N_{coll} are particularly important for normalisation purposes—soft probes (low energy transfer) are expected to scale proportionally with the N_{part}, whereas hard probes (high energy transfer) with the N_{coll} [1].

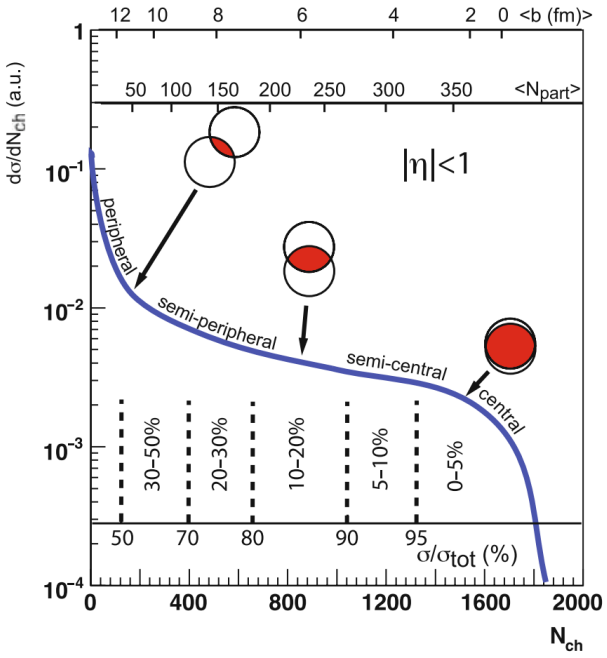

Fig. 1.1: Cartoon of a distribution in final-state charged particle multiplicity. Connections with centrality, b, and $\langle N_{\text{part}} \rangle$ can be seen. Taken from [3].

Mentioned variables, however, are not physically measurable. One thus also works with centrality, a percentage of the total nuclear interaction cross section. It is inferred usually from the total transverse energy E_{T} or the particle density N_{ch} (multiplicity) and Monte Carlo simulations using the Glauber model [2]. The approximate relations between the centrality, b, N_{part}, N_{ch}, and the collision geometry are illustrated in Fig. 1.1.

1.1.3 Quark-gluon plasma

Lattice QCD calculations predict that under extreme temperatures, hadronic matter undergoes a phase transition and becomes a plasma of deconfined quarks and gluons (QGP). Observations of a strongly interacting near-perfect liquid (sQGP) have been made in the early 2000's in heavy-ion collisions at the RHIC collider in Brookhaven National Laboratory. Its signatures are consistent with those of the QGP. Illustration of the space-time evolution of a such heavy-ion collisions with QGP is shown in Fig. 1.2.

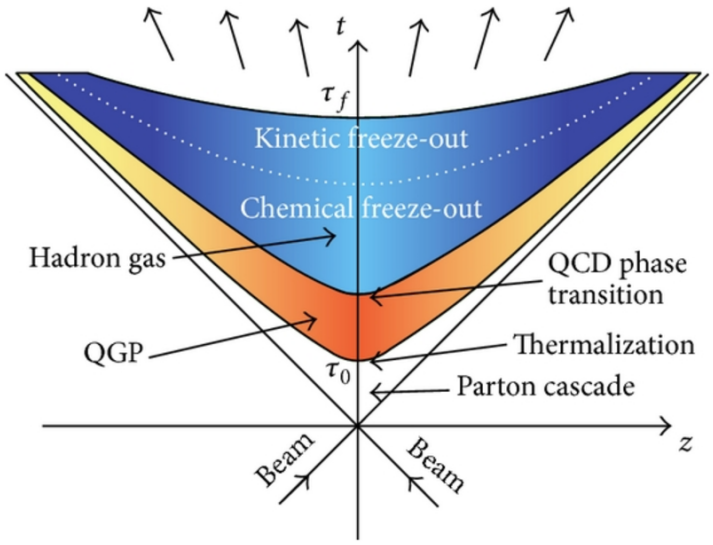

Fig. 1.2: Space-time evolution of a heavy-ion collision with expected creation of the quark-gluon plasma. Taken from [8].

Studies of the QGP are of great importance. For instance, QGP is believed to comprise the universe a few microseconds after the Big Bang [6]. Therefore, measurements of the QGP properties and determination of e.g. its equation of state have large implications for early-cosmological models. Moreover, QGP studies also bring valuable insights on phenomena in the non-perturbative regimes of QCD, such as the hadronisation. That being said, the QGP is still a large unknown. Of what type is the phase transition from hadronic matter to QGP? How does the fireball of deconfined quarks and gluons transforms into a hadron gas? Is there a restoration of chiral symmetry? These are only some of the plethora of unanswered questions.

1.2 Heavy quarkonia

Quarkonium is a neutral meson consisting of a quark and an anti-quark of the same flavour. Charm quarkonia (*charmonia*) and bottom quarkonia (*bottomonia*) exist in various states which vary in mass and binding energy. Overview of these can be found in Tab. 1.1.

States	J/ψ	χ_c	ψ'	$\Upsilon(1S)$	χ_b	$\Upsilon(2S)$	χ_b'	$\Upsilon(3S)$
Mass [GeV]	3.07	3.53	3.68	9.46	9.99	10.02	10.26	10.36
Binding energy [GeV]	0.64	0.20	0.05	1.10	0.67	0.54	0.31	0.20
Radius [fm]	0.25	0.36	0.45	0.14	0.22	0.28	0.34	0.39

Tab. 1.1: Mass, binding energy, and radii of common quarkonia states of the charm and the bottom family. Taken from [3].

The heavy quarkonia are a crucial probe to the QGP existence and its properties, since their production is hypothesised to be significantly suppressed if the deconfining medium is present, due to its colour screening effect [4]. This is further facilitated by the fact that the production cross section of the constituent $c\bar{c}$ or $b\bar{b}$ quark pairs are well-calculable in perturbative QCD [6]. Furthermore, the ground states—the J/ψ and the Υ(1S)—have binding energies considerably above the expected QGP temperature and their lifetime is also significantly longer than that of QGP. Finally, the quarkonia have easily detectable di-lepton decay channels [5].

1.2.1 Debye colour screening of the binding potential

In a deconfining medium, quarkonium system cannot be bound due to the Debye-like dissociation caused by the screening by free colour-charge carriers.

For the sake of simplicity, let us assume that the binding potential of a quarkonium with radius r, placed in a finite-temperature T QCD medium, takes the form of

$$V(r,T) = \kappa r_D(1 - e^{\frac{-r}{r_D}}) - \frac{4\alpha_s}{3} \cdot \frac{e^{\frac{-r}{r_D}}}{r} \ , \tag{1.4}$$

where $r_D = r_D(T)$ is the Debye radius which characterises the screening effect, κ the string tension coefficient, and α_s the strong coupling constant. The Debye radius can be calculated based on pQCD [7] and goes as follows

$$r_D(T) = \sqrt{\frac{1}{6\pi\alpha_s}}\frac{1}{T} \ . \tag{1.5}$$

Event at	RHIC 200 GeV	LHC 2.76 TeV
$N_{c\bar{c}}$/event	13	115
$N_{b\bar{b}}$/event	0.1	3

Tab. 1.2: Estimated number of heavy quark pairs created per central collision event (0-10%) at RHIC and LHC energies [12].

One can then use the potential (1.4) in the system Hamiltonian and set it equal to the total system energy $E(r)$. The function $E(r)$ has a minimum in r only if $r < r_D$. This translates to the following—a quarkonium system can be bound only if its radius r is smaller than the Debye screening radius r_D [7].

1.2.2 Other behaviour of the quarkonium

Sequential melting

Since the different quarkonium states vary in their binding energies, and thus their radii, the dissociation happens for different values of r_D. Because of the fact that $r_D(T) \propto 1/T$, the various states are expected to become unbound at different temperatures. This has been proposed as a "QGP thermometer" [9]—by measuring the suppressed production of different quarkonium states, constraints on the QGP temperature can be inferred. Estimates on the quarkonium states' dissociation temperatures are presented in Fig. 1.3.

Statistical recombination

If abundant enough, the deconfined heavy quarks can randomly coalesce at the QGP phase boundary and form a quarkonium state—thus enhance the measured production. This significantly complicates interpretation of the suppression caused by the colour screening. Thanks to the scarcity of the b and $\bar{b}$ quarks in a typical Au+Au collision of $\sqrt{s_{\mathrm{NN}}} = 200$ GeV, the regeneration caused by recombination is negligible for the bottomonia at RHIC [11]. For the charmonia at RHIC or for the charmonia and bottomonia at the LHC, this is not valid. For the approximate number of heavy-quark pairs in a heavy-ion collision, refer to Tab. 1.2.

Cold nuclear matter (CNM) effects

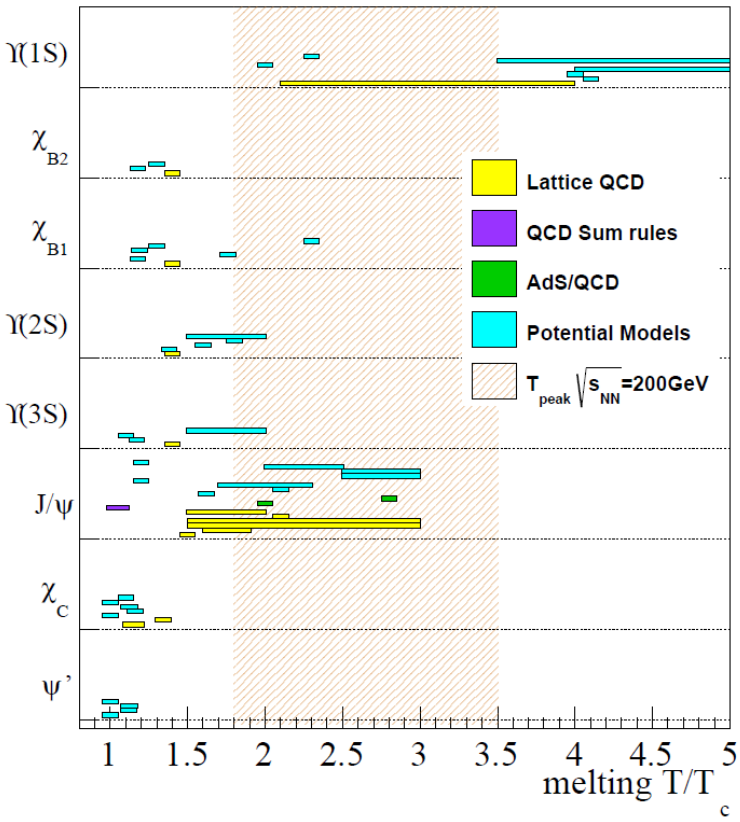

Fig. 1.3: Ratios of the quarkonium melting temperature T and the QGP critical temperature T_C calculated by a variety of models. The shaded band denotes the estimation for the peak QGP temperature in Au+Au collisions of $\sqrt{s_{\rm NN}} = 200$ GeV at RHIC. Taken from [10].

The CNM effects are effects that also come into play in heavy-ion collisions but are unrelated to the hot QGP phase. These can be changes to the initial state, like the nuclear (anti-)shadowing or initial state energy loss. Final state inelastic interactions with the nuclear remnants or the co-moving hadrons also belong to these [6]. One method to study the CNM effects is to measure the quarkonium production in hadron-nucleus (eg. p+Au) collisions. It can be shown that the bottomonia at RHIC have negligible susceptibility to the co-mover absorption [13].

Feed-down

The quarkonium ground states have a significant contribution from the decays of higher excited states. For instance, as much as 50% of the Υ(1S) can come from the feed-down [5]. Naturally, suppression of the excited states then also leads to some suppression of the lower state. Because of the fact that many of the higher states are virtually unmeasurable (eg. the p-wave states), this creates a big source of uncertainty and must be carefully taken into account.

1.2.3 Nuclear modification factor

Difference in the production between proton-proton collisions and heavy-ion collisions is quantified via the nuclear modification factor R_{AA}. It is equal to unity if no net medium effects are observed and zero if complete suppression is measured. For hard probes, in its simplest form, it is defined as follows,

$$R_{\mathrm{AA}} = \frac{Y_{\mathrm{AA}}}{N_{\mathrm{coll}} \times Y_{\mathrm{pp}}} \ , \tag{1.6}$$

where Y_{AA} and Y_{pp} are adequately normalised quarkonium yields in A+A and p+p collisions, respectively.

Chapter 2

Experimental setup

This chapter provides an overview on the experimental facility used in the acquisition of the data for the analysis presented in this project. In the first part, the accelerator is presented. Subsequently, the detector and its notable sub-systems are described.

2.1 The RHIC accelerator facility

The Relativistic Heavy Ion Collider is a heavy-ion accelerator located at the Brookhaven National Laboratory (BNL) in New York, USA. The RHIC facility and its experiments have been essential in the investigation of heavy-ion collisions and searches for the QGP. The ions are accelerated in two separate storage rings, which intersect at six interaction points. As of now, only one of the points is used—by the STAR experiment. In the past, however, the PHENIX, PHOBOS, and BRAHMS experiments were present, all of which have completed their data-taking.

At RHIC, heavy ions can be accelerated up to $\sqrt{s_{\mathrm{NN}}} = 200$ GeV. Thanks to its ion source, various ions can be accelerated—besides the normally used gold, collisions of nuclei of, for instance, uranium or copper have also been measured. Another important feature is the option to change the collision energy of the ions. This was utilised in the Beam Energy Scan (BES) programme, which is important in studying the QCD phase diagram. Furthermore,

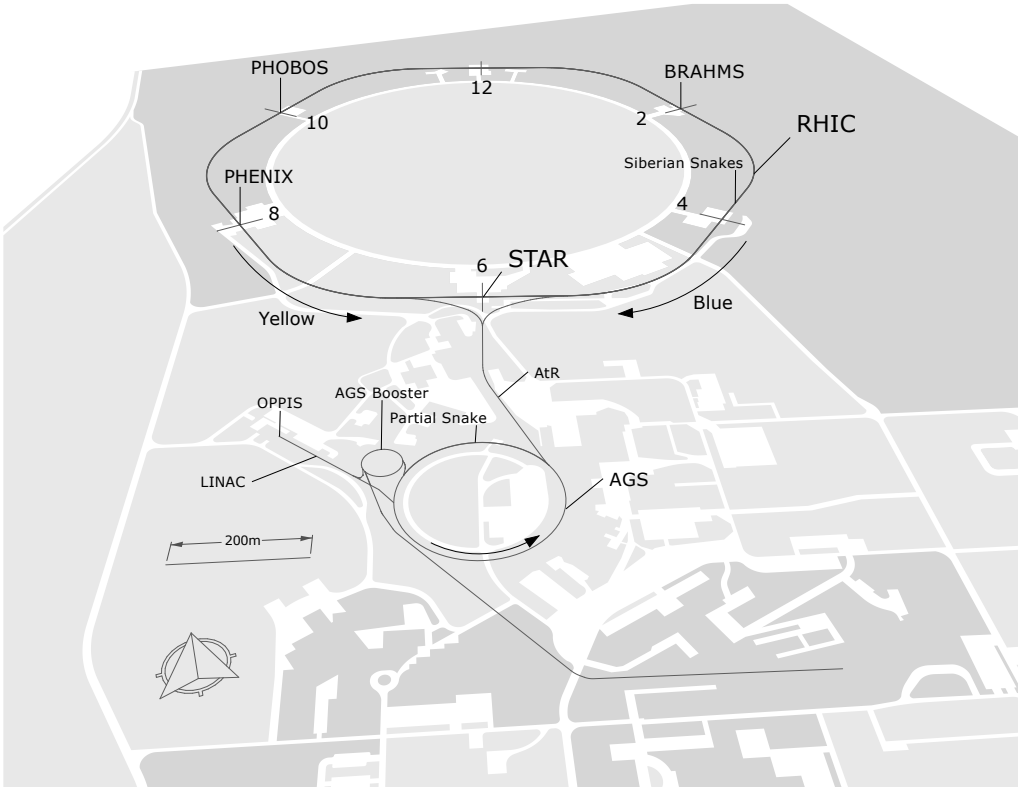

Fig. 2.1: Depiction of the RHIC accelerator complex. Taken from [15].

proton beams can be collided. These can be polarised, which makes RHIC the most powerful polarised proton beam accelerator in the world.

The layout of the accelerator complex can be seen in Fig. 2.1. For detailed information on the accelerating procedure and beam characteristics, refer to [14].

2.2 The STAR experiment

The Solenoidal Tracker At RHIC is a multi-purpose heavy-ion collisions detector with full coverage in azimuth ($0 < \varphi < 2\pi$) at mid-rapidity ($|\eta| < 1$). Thanks to its excellent PID capabilities and constant upgrades, STAR still belongs to the world's leading heavy-ion experiments. Majority of the detector is surrounded by a solenoidal magnet system, which subjects it to a magnetic field of 0.5 T, parallel to the beam-line. The STAR experiment can be seen in Fig. 2.2. Some of its most prominent sub-systems are:

- Time Projection Chamber (TPC),
- Barrel Electromagnetic Calorimeter (BEMC),
- Time Of Flight detector (TOF): greatly improves PID capabilities for particles with momentum up to 3 GeV/c by measuring its velocity β,
- Muon Telescope Detector (MTD): located behind the magnet, this detector provides PID and triggering-on for muons,
- Heavy Flavor Tracker (HFT): a silicon detector placed as close as 2.5 cm from the beam-pipe, which improves secondary vertex resolution up to ~ 40 μm,
- Vertex Position Detector (VPD): a quick coincidental detector used for triggering and on-line determination of a primary vertex position.

The two detectors most relevant to the presented study—the TPC and the BEMC—are described in more detail further in the chapter.

2.2.1 Time Projection Chamber

The TPC [16] is the primary tracking detector within STAR. This 4.2 m long cylinder with 2 m outer radius is also responsible for primary vertex reconstruction and provides PID via ionisation energy loss. The chamber is filled with a mixture of argon (90%) and methane (10%) and operated 2 mbar above the atmospheric pressure. A thin high voltage membrane of -28 kV is situated at $z = 0$ and together with grounded end-caps provides a homogeneous electric field of 135 V/cm. This field causes the electrons from the ionisation to drift at a constant velocity of 5.5 cm/μs, which results in the maximum drift time of ~ 40 μs. The detector is illustrated in Fig. 2.3.

The electrons are collected and read-out at the end-caps via the Multi-Wire Proportional Chambers (MWPCs). They are divided into 12 sectors and each of these holds 45 pad-rows, 13 in the inner region and 32 in the outer. The inner region has continuous pad coverage to facilitate the $\mathrm{d}E/\mathrm{d}x$ measurement. The inner region has smaller pads to provide a better

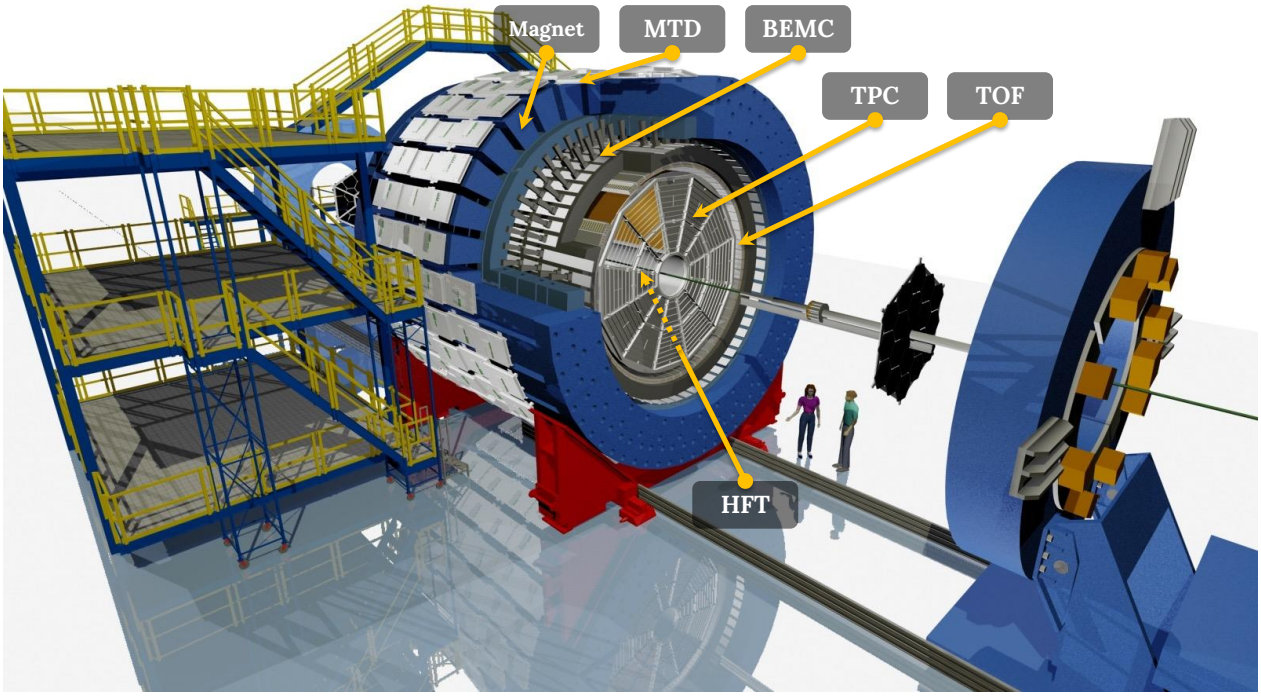

Fig. 2.2: Illustration of the STAR detector and some of its subsystems. Reproduced from [15].

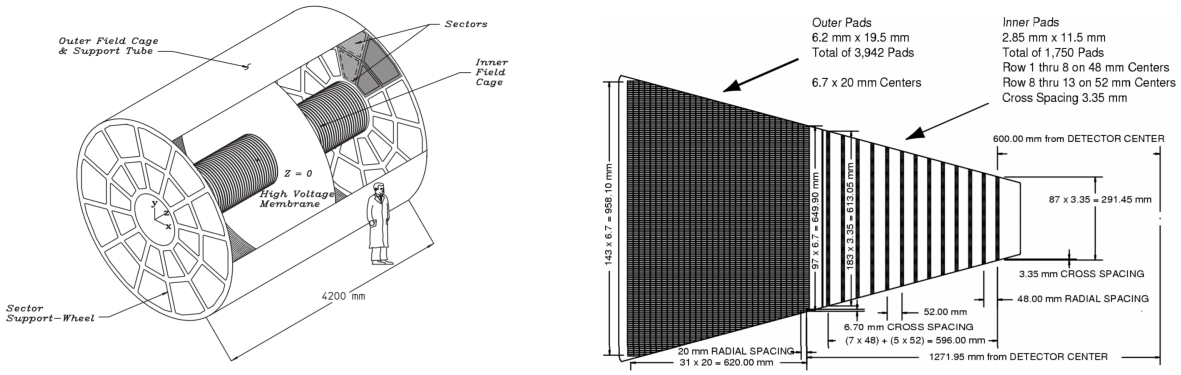

Fig. 2.3: Picture of the (left) TPC detector; (right) one of the end-cap MWPC sectors. Taken from [16].

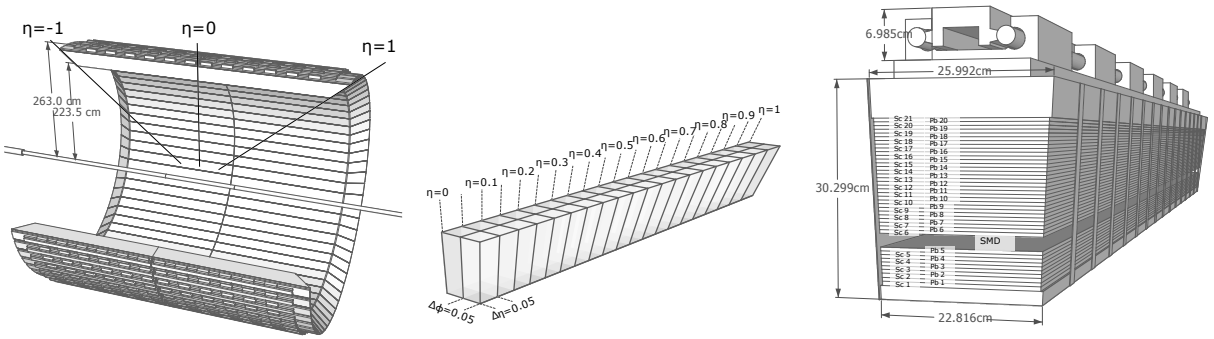

Fig. 2.4: Illustration of the (left) STAR BEMC detector; (middle) a BEMC module geometry; (left) layout of BEMC towers. Taken from [15] [17].

resolution for the higher track densities. The sector and its parameters can be seen in Fig. 2.3.

2.2.2 Barrel Electromagnetic Calorimeter

The BEMC [17] is a fast sampling calorimeter system situated behind the TPC and the TOF detectors, sharing their azimuthal and pseudorapidity coverage. It is used for triggering, detection of photons, and PID of mainly electrons via E/pc. The trigger operates on a high-tower principle, with a three-level customisable threshold.

The barrel's inner radius is ~ 2.2 m and its outer radius ~ 2.5 m. The detector consists of 120 modules, each holding 2×20 cells—the towers. One tower has a coverage of $\Delta\varphi \times \Delta\eta \simeq 0.05 \times 0.05$. They are composed of 21 scintillator tiles (created by light-insulating the module 'megatiles' tower-by-tower), interleaved with 20 lead absorber plates. Cells of the Barrel Shower Maximum Detector (BSMD)—which improves the spatial and shape resolution of the produced shower—are situated between the fifth and the sixth layer. Light from the scintillator tiles are collected by the means of Wavelength Shifting Fibres (WLS), connecting to clear optical fibres, and then read-out by Photo-Multiplier Tubes (PMT). The geometry of the BMC and its modules, as well as a layout of BEMC towers, is displayed in Fig. 2.4.

Chapter 3

Author's analysis on $\Upsilon \to e^+e^-$

This chapter is the principal part of this report and overviews the author's analysis on the Υ meson production using the di-electron channel. In the beginning, the data sample and reconstruction methods are explained. Then, reconstruction efficiencies are introduced. Finally, the signal extraction methods and the yields are presented.

3.1 Data

This analysis has been carried out on the data collected in 2014 with the STAR experiment from Au+Au collisions of $\sqrt{s_{\mathrm{NN}}} = 200$ GeV. BHT2 trigger (high-tower trigger with ADC signal threshold 19) was used to ensure rich abundance of events with hard electrons. A total of 118.9 M BHT2 events were analysed, which corresponds to the integrated luminosity of ~ 4.1 nb^{-1}.

Originally, data reconstructed with the newer production tag P16d were used, as opposed to the older tag P15c, since it included a fix on the HFT tracking algorithm. Even though the analysis does not implement HFT directly, this could still result in a slightly better tracking efficiency for primary tracks. Nonetheless, the P16d tag did not include a dataset with high-luminosity configuration, which contains a significant fraction ($\sim 50\%$) of the BHT2 events. For this reason, results coming from the P15c data are presented in this report.

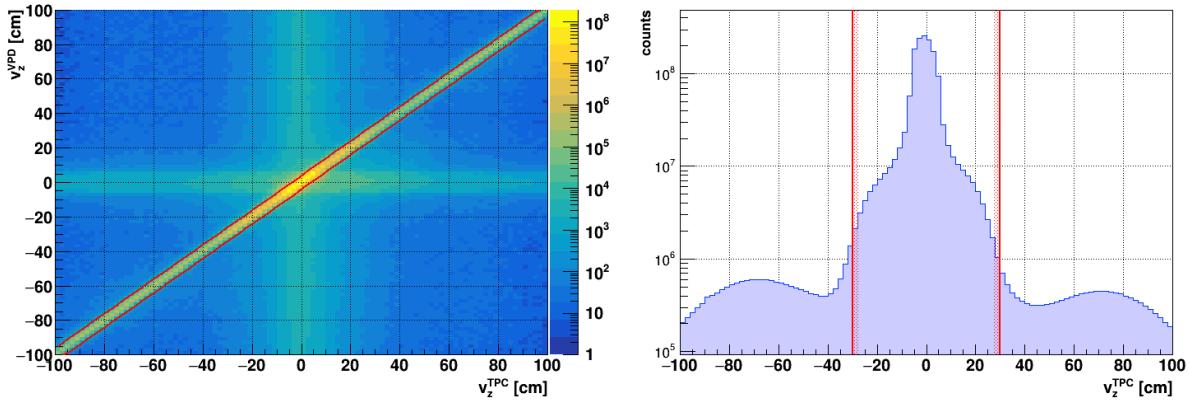

Fig. 3.1: This analysis: Distributions of the z-coordinate of the primary vertex v_z^{TPC} vs. the v_z^{VPD} (left) and the v_z^{TPC} (right). The red lines denote the applied cuts.

3.1.1 Event selection

Following set of criteria was applied on the events:

- $|v_z^{TPC}| < 30$ cm—z-coordinate of the event TPC-reconstructed primary vertex,
- $|v_z^{TPC} - v_z^{VPD}| < 4$ cm—difference between z-coordinates of the TPC-reconstructed and VPD-reconstructed primary vertices,
- the event is BHT2-triggered.

Distributions of the inclusive events' v_z^{TPC} and v_z^{VPD} with the applied cuts are plotted in Fig. 3.1.

3.1.2 Event centrality

At STAR, centrality is calculated from the reference multiplicity *grefMult*, which is the number of charged particles at $|\eta| < 0.5$ and the shortest distance from the primary vertex DCA$<$ 3 cm. The *grefMult*, however, needs to be corrected to account for run-dependent TPC inefficiencies. This is done via the STAR Library class *StRefMultCorr*. This class is also used to calculate the centrality classes. A centrality class of eg. $0-10\%$ corresponds to the $0-10\%$ most central collisions.

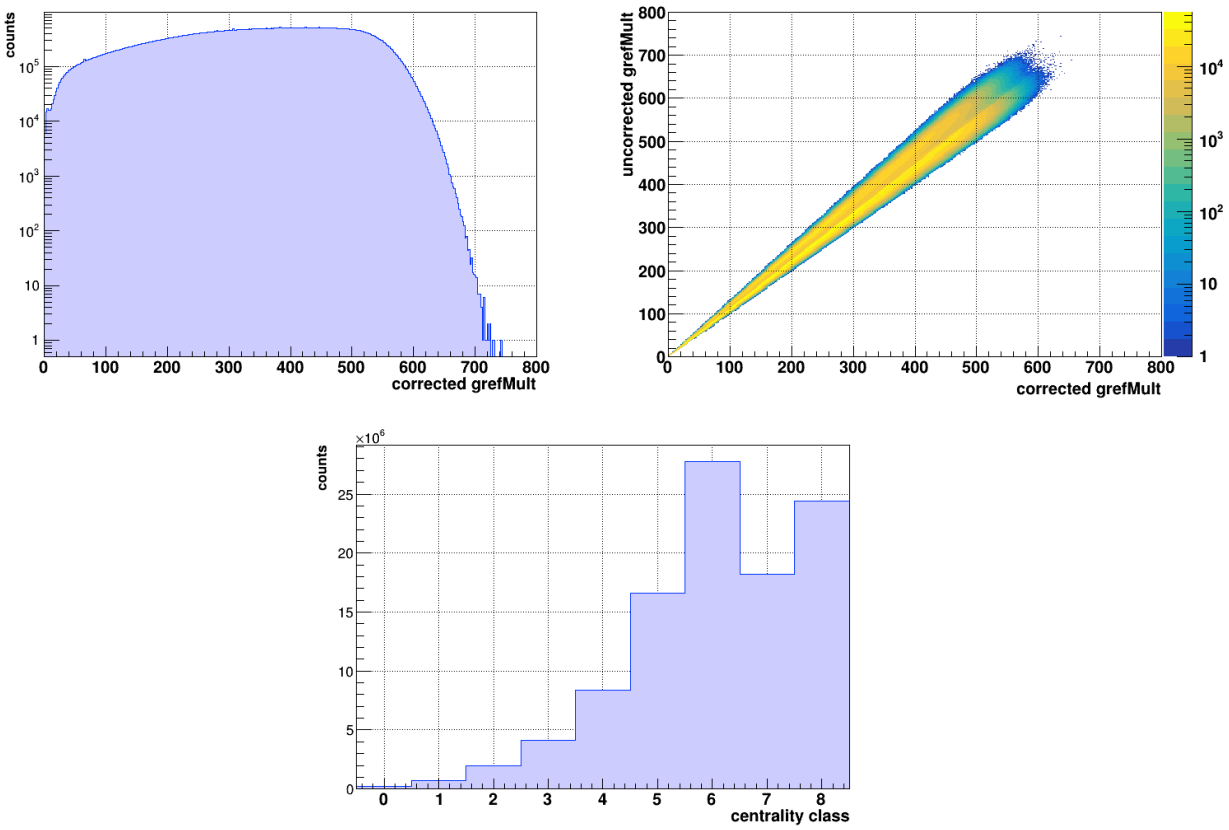

Fig. 3.2: This analysis: Distributions of the corrected reference multiplicity *gefMult* (left); corrected *grefMult* vs. the uncorrected *grefMult* (right); and the centrality classes (bottom). The class 8 corresponds to $0-5\%$ of the most central collisions, class 7 to $5-10\%$, class 6 to $10-20\%$, and the other classes similarily, with an increment of 10%.

Distributions of the corrected and uncorrected multiplicities as well as the centrality classes for the selected events can be seen in Fig. 3.2. It is noteworthy that the centrality distribution is not uniform, which is seemingly inconsistent with the definition of the classes. This, however, comes from using the BHT2-triggered events, which are generally biased towards more central collisions.

3.1.3 MC data with embedded Υ

For various purposes—particularly the study of reconstruction efficiencies and detector effets—it is useful to work with a Monte Carlo generated data sample. Such sample is made so that it resembles the real measured events as well as possible, but is artificially enhanced with the sought signal. Such datasets—called "embedding"—can be then analysed with the same reconstruction methods as with the real data and its results compared with the a priori known MC truth.

The events are generated with a PYTHIA-based event generator and the particle propagation and reconstruction is simulated via GEANT [18]. The sample was created with these parameters:

- 900 K events—300 K for each Υ state,
- particles per events: 5% of multiplicity,
- 1 Υ per event, generated with flat distribution in $|y| < 1.2$, $\varphi < 2\pi$, and $0 < p_{\mathrm{T}} < 10$.

3.2 Upsilon reconstruction

This analysis utilises the di-electron decay channel of the Υ, although reconstruction via di-muons is also possible thanks to the installation of MTD in 2014. The electrons are identified with a combination of TPC and BEMC. A TPC-reconstructed primary track must be successfully matched to a cluster within BEMC. A BEMC cluster is defined as a collection of three neighbouring BEMC towers with the highest measured charge. At least one of the two electron daughters must also be matched to the tower which fired the BHT2 trigger. A simple cartoon of the reconstruction is shown in Fig. 3.3.

3.2.1 Selection with TPC

Charged particle tracks reconstructed via TPC are subjected to the following set of cuts:

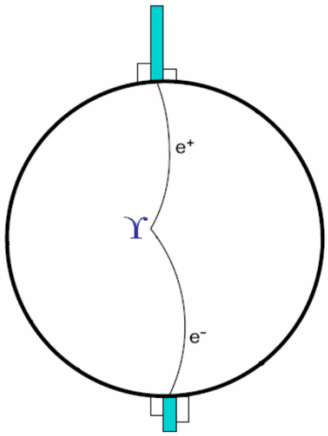

Fig. 3.3: Cartoon of the employed reconstruction algorithm. The curved lines represent the TPC tracks and the columns denote the BEMC towers.

- the track is a primary track, i.e. matched to the primary vertex,
- *nHitsFit* ≥ 25—hit-points in TPC used for the track fitting,
- *nHitsdEdx* ≥ 10—hit-points in TPC used for the $\mathrm{d}E/\mathrm{d}x$ determination,
- *nHitsRatio* ≥ 0.52—ratio of the hit-points used and the possible maximum in a given TPC sector,
- DCA< 1.5 cm—distance of closest approach to the primary vertex
- $-1.5 < n\sigma_e < 3$—number of Gaussian deviations from the predicted $\langle \mathrm{d}E/\mathrm{d}x \rangle$ value for electrons,
- $|\eta| < 1.0$,
- $p > 3.5$ GeV,
- $p > 4.5$ GeV for at least one daughter,
- $|y| < 1$ for a daughter pair,
- $p_{\mathrm{T}} < 10$ GeV for a daughter pair.

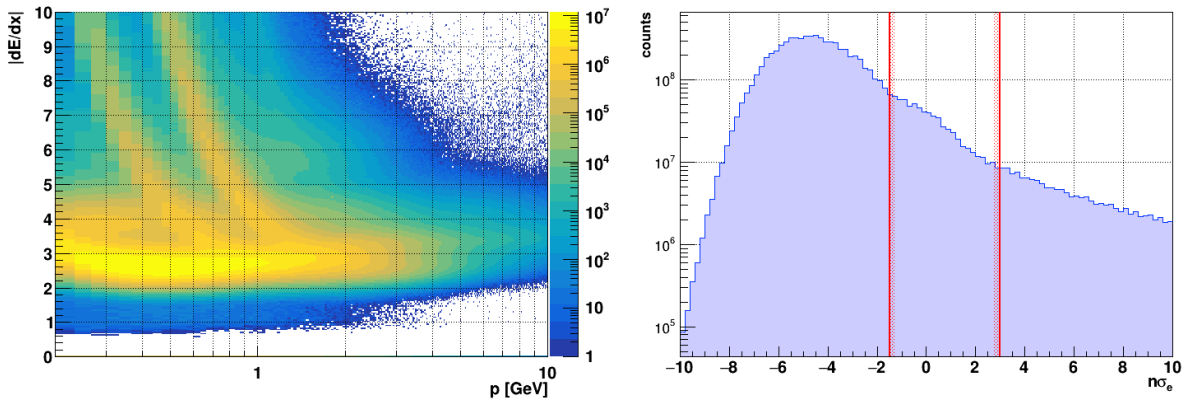

Fig. 3.4: This analysis: Distributions of the TPC tracks energy loss $\mathrm{d}E/\mathrm{d}x$ vs. primary momentum p (left); and the $n\sigma_e$ (right). Red lines represent the applied cuts. The notable yellow structures in the $\mathrm{d}E/\mathrm{d}x$ plot belong to the pions, electrons, kaons, and protons, going from bottom left to top right.

Distributions of the $\mathrm{d}E/\mathrm{d}x$ vs. p and of the $n\sigma_e$ with the applied cut are shown in Fig. 3.4. The kinematics variables—η, φ, and p—are plotted in Fig. 3.5. The peak at zero corresponds to the tracks that are not primary. Finally, the daughter pair kinematics—p_T and y—can be found in Fig 3.6.

3.2.2 Selection with BEMC

The BEMC is used for both triggering and PID. A triggered high-tower must have exceeded or been equal to a threshold of 19 on its ADC value. A distribution of the ADC values of all 4800 BEMC towers can be seen in Fig. 3.7 (left). It is apparent from the plot that some towers fire significantly more often than others. These "hot towers" can be corrected for based on a careful run-by-run analysis.

PID traits given by the calorimeter are not based on single towers but on clusters of three neighbouring towers with the highest ADC value. A TPC track successfully matched to such cluster needs to subsequently fulfil following conditions:

- $0.3 < E/p < 1.8$—deposited energy in a cluster divided by the track momentum,

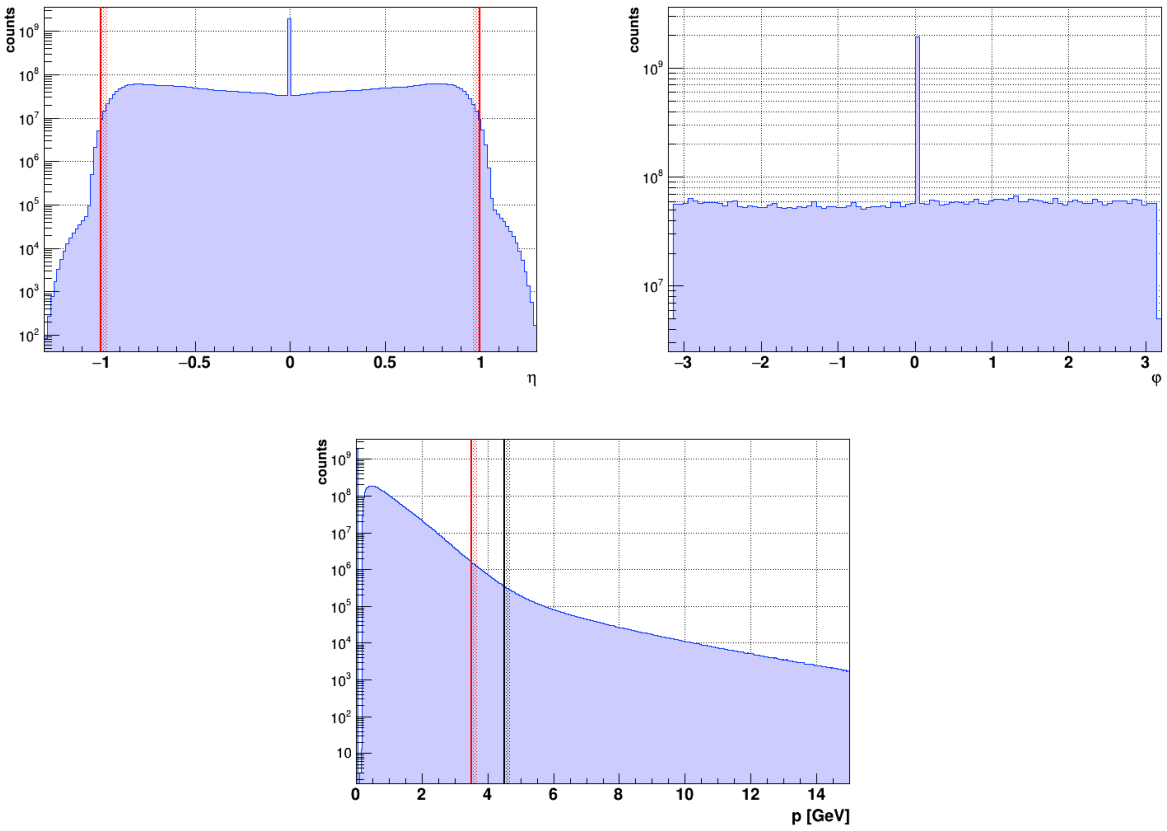

Fig. 3.5: This analysis: Distributions of the pseudorapidity η (left); azimuthal angle φ (right); and the momentum p (bottom). The peak at η,$\varphi = 0$ corresponds to the non-primary tracks. The red lines denote the applied cuts for all candidates, the black line represents the cut for at least one of the daughters in a pair.

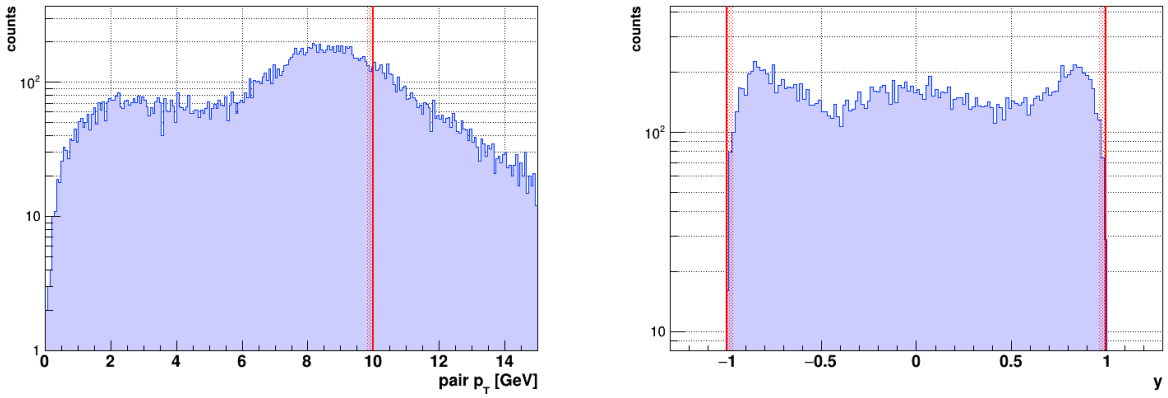

Fig. 3.6: This analysis: Distribution of the kinematics variables of the daughter pair—pair transverse momentum p_{T} (left) and pair rapidity y (right). The red lines represent the chosen selection cuts.

- $|zDist| < 5$ cm—cluster distance in the z-direction,
- $|phiDist| < 0.05$ cm—cluster distance in th φ-direction,
- the leading tower of a matched cluster = BHT2-triggered tower, for at least one track.

The BEMC-related distributions and cuts can be found in Fig. 3.7 and Fig. 3.8.

3.3 Reconstruction efficiency

Knowledge of the total reconstruction efficiency for the Υ is crucial in order to determine the true production. Combining the detector acceptance, the kinematics cuts, and the tracking efficiency gives us a value of $\sim 10\%$ solely, as can be seen in the embedding. The final value is expected to be ca. $3 - 5\%$.

3.3.1 Single electron $n\sigma_e$ efficiency

The $n\sigma_e$ cut efficiency can be determined from the real data instead of simulations. It is the fraction of electrons which pass the $n\sigma_e$ cut. The predicted mean value for energy loss

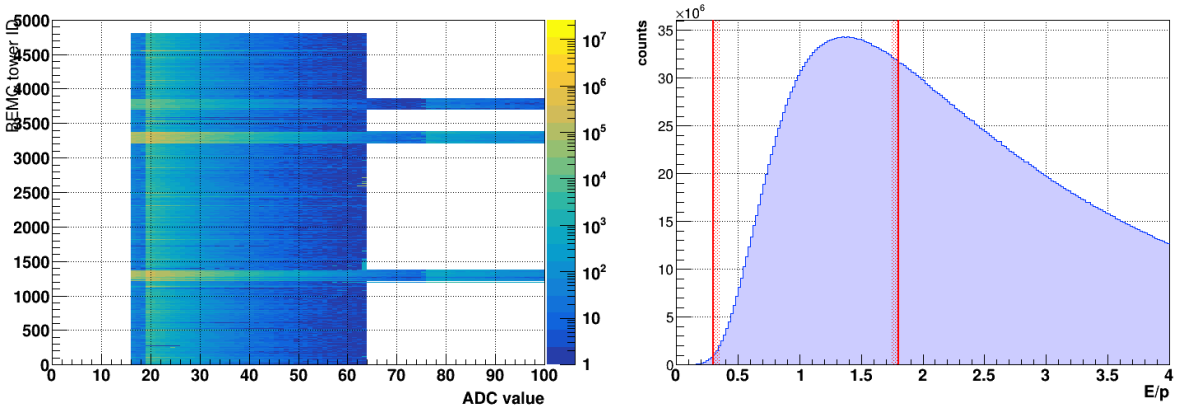

Fig. 3.7: This analysis: Distributions of the BEMC BHT2-triggered towers and their corresponding ADC value (left); and the energy over momentum E/p (right). The red lines denote the applied cuts.

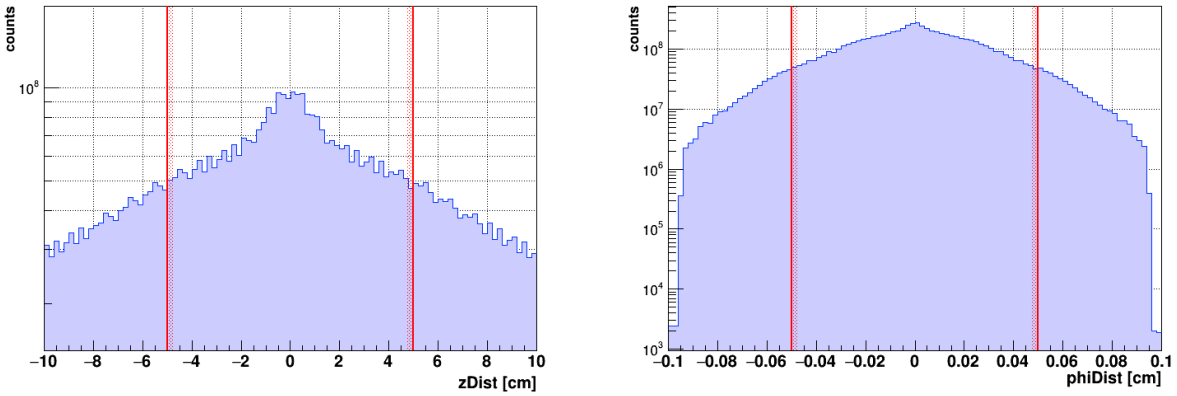

Fig. 3.8: This analysis: Distributions of the cluster distance in the z-direction (left); and the φ-direction. The red lines represent the chosen cuts.

$\langle \mathrm{d}E/\mathrm{d}x \rangle$ of electron in TPC is given by its p-dependent Bichsel function. The measured $\mathrm{d}E/\mathrm{d}x$ should follow a normal distribution centered in this function. The $n\sigma_e$ is constructed so that at any p it gives the distance between the $\mathrm{d}E/\mathrm{d}x$ and the mean in number of σ of said normal distribution. Ideally, the $n\sigma_e$ distribution for electrons should be a Gaussian with $\mu = 0$, $\sigma = 1$. However, this is not true (usually $\mu \sim -0.5$, $\sigma \sim 1$) and thus must be carefully determined.

In first attempt, the efficiency was determined with single identified electrons. All TPC and EMC cuts were included except the $n\sigma_e$. The $n\sigma_e$ spectrum is then constructed for several p_{T} bins and in each of these, fitted with three Gaussians corresponding to the pion, kaon+proton, and electron peaks. To avoid the μ-σ correlation, all widths were constrained to vary from their mean by 3 errors of the mean.

Three of the p_{T} bins of $n\sigma_e$ distributions with fits, as well as the final $n\sigma_e$ efficiency as a function of p_{T}, are shown in Fig. 3.9. Due to the extreme amount of pions, the fits are not very stable. A clean photonic electron sample of e.g. $m_{ee} < 100$ MeV can be used to determine the efficiency with a better precision and stability.

3.4 Signal extraction

From pairs of oppositely charged TPC- and BEMC-identified electrons, the invariant mass spectrum is constructed. A clear Υ signal is observed, as can be seen in Fig. 3.12. Limited statistics, low momentum resolution at high-p_{T}, and additional background sources complicate the extraction of pure Υ signal from the spectrum. A careful fitting must be employed instead of simple bin-counting.

3.4.1 Signal peaks

Parametrisations of the Υ(1S), Υ(2S), and Υ(3S) signal shape functions are obtained by fitting the mass peaks of the three states in the embedding data, which, for the ground state, is shown in Fig. 3.10 (left). The Crystal-Ball function is used for each state. The result from

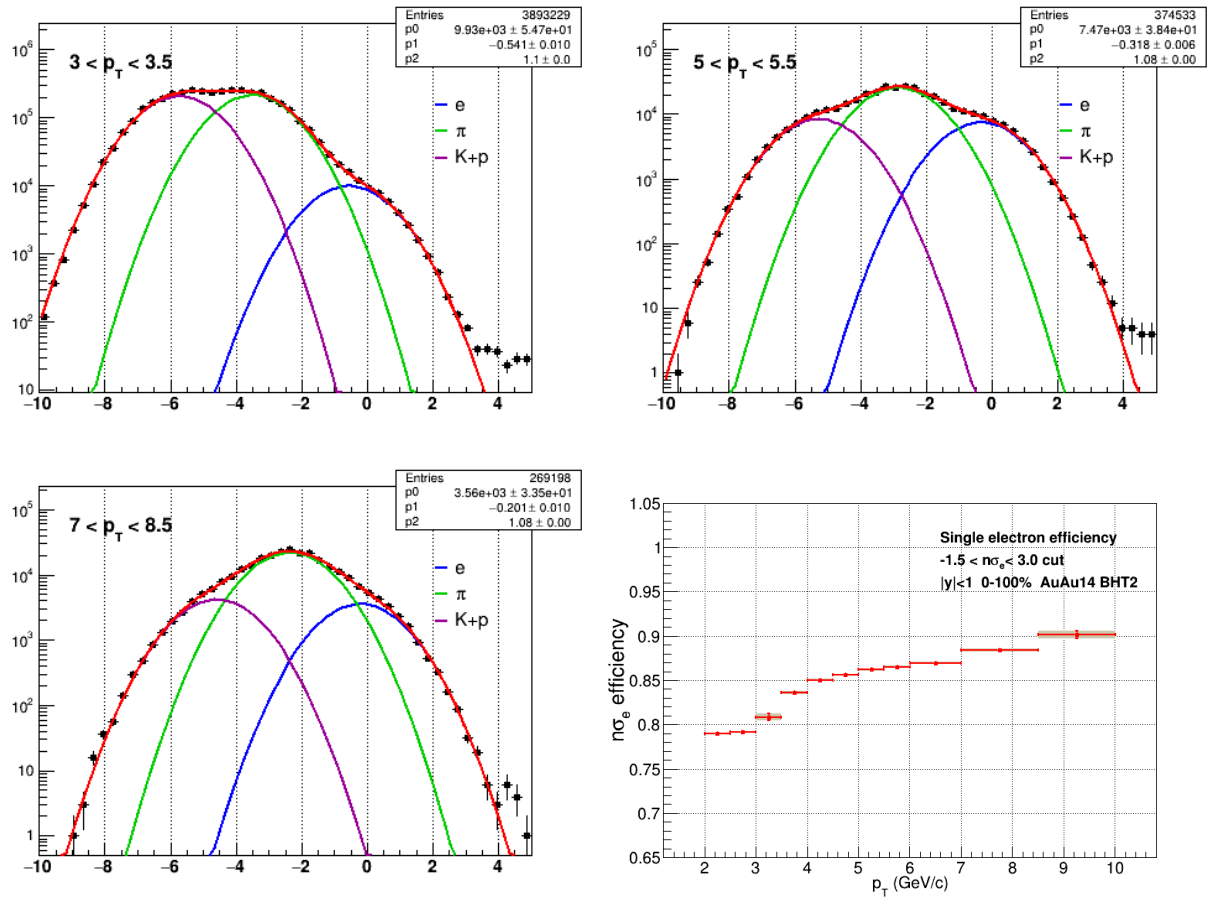

Fig. 3.9: This analysis: The $n\sigma_e$ distribution for single identified electrons with three Gaussian fits for electrons, pions, and kaons and protons in a $3 < p_{\mathrm{T}} < 3.5$ GeV bin (top left), $5 < p_{\mathrm{T}} < 5.5$ GeV bin (top right), $7 < p_{\mathrm{T}} < 8.5$ GeV bin (bottom left). The resulting $n\sigma_e$ efficiency as a function of p_{T} is also shown (bottom right).

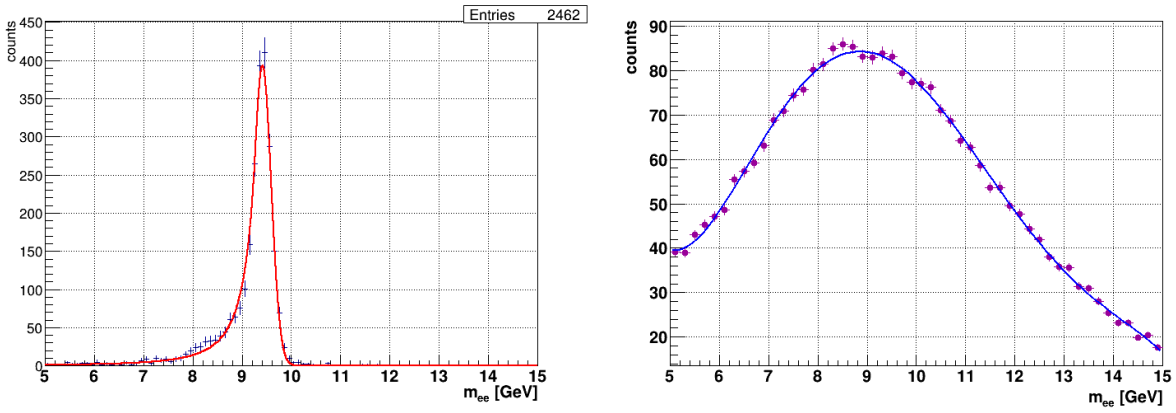

Fig. 3.10: This analysis: The fitting function template for the $\Upsilon(1S)$ (left), where the Crystal-Ball function is used; and the combinatorial background via the event-mixing method (right), where a fifth-order polynomial is employed.

simulations gives a good prediction on the signal shape. Further corrections needed due to imperfections of the simulation can be determined by comparing the J/ψ mass peak in the embedding to the one in the real data, where it is abundant enough to give an unambiguous fit.

3.4.2 Combinatorial background

Due to the character of the reconstruction—random pairing of any two electrons—the biggest source of background is the combinatorial background of uncorrelated electrons. The like-sign method assumes that the chance to pair two uncorrelated daughters is not dependent on their sign. The invariant mass spectra are thus also built from two positive daughters and from two negative daughters. The spectra are then added together and can be used to estimate this background. A third-order polynomial is used as a fitting function.

Another method is the event-mixing method. There, the random pairing of uncorrelated daughters is achieved by selecting each daughter from a different event. Ideally, characteristics of these events should be as similar as possible. Currently, the mixing is done across events in the same v_z-classes. Splitting the events in e.g. the multiplicity can also be considered.

Invariant mass spectrum from oppositely charged daughters coming from different events and a fifth-order polynomial fit are plotted in Fig. 3.10 (right).

3.4.3 Physical background

Apart from the combinatorics, the invariant mass spectrum is also contributed to by electron-positron pairs coming from real physical processes. The two most important ones are the $B\bar{B}$ semi-leptonic decays and the Drell-Yan di-lepton continuum. It is important to parametrise the shapes of these backgrounds, and preferably, also their magnitude.

In first approximation, the $b\bar{b} + ... \to B\bar{B} + ... \to e^+e^- + ...$ background is simulated with Pythia8 [19] in p+p collisions at $\sqrt{s} = 200$ GeV. The final-state electrons are smeared with p_{T}-dependent smearing functions determined from the embedding to account for detector effects. They are then reconstructed the same way and with the same cuts as the Υ in the real data. This is done so that the resultant spectrum shape acquires the same bias coming from the distribution of the kinematic variables. The $B\bar{B}$ background shape fitted with a ratio of two power laws can be found in Fig. 3.11 (left).

The Drell-Yan process, $q\bar{q} \to \gamma^*/Z^* \to e^+e^-$ also contributes to the background. It can be simulated with Pythia or Herwig. Example of an event generated with Herwig6 [20] is illustrated in Fig. 3.11 (right).

3.4.4 Total fit and yield extraction

A composite function—including the three Υ states peaks, the combinatorial background, and the $B\bar{B}$ background function shapes—is used to fit the invariant mass spectrum. Both the like-sign and the event-mixing methods are employed. The Υ function parameters are allowed to vary within 3σ from the values determined from embedding. Their amplitudes are let completely free. The $B\bar{B}$ and the event-mixing combinatorial background are both fixed from their previous fits, also except for their amplitudes. The like-sign combinatorial background is fixed altogether.

The invariant mass spectra with the total fits using both combinatorial background esti-

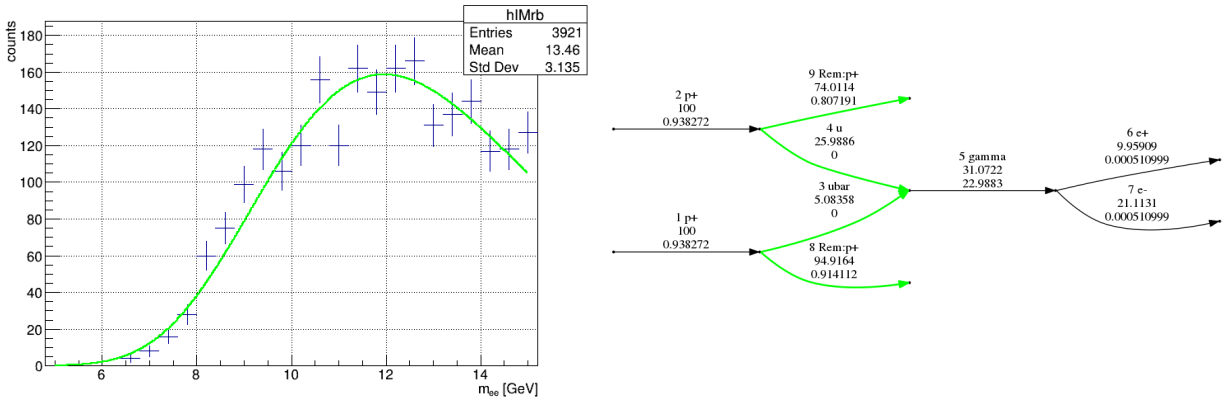

Fig. 3.11: This analysis: A sample of the Pythia8-simulated $B\bar{B}$ background with a third-order polynomial fit template (left); and a display of a Drell-Yan event in Herwig6 (right).

mation methods are plotted in Fig. 3.12. For the ground $\Upsilon(1S)$ state, a yield of 383 ± 44 is observed for the like-sign method, and 367 ± 64 for the event-mixing method. An estimation of the Drell-Yan background and possibly also corrections for the Υ templates are further needed to reduce the large uncertainties on the extracted yield.

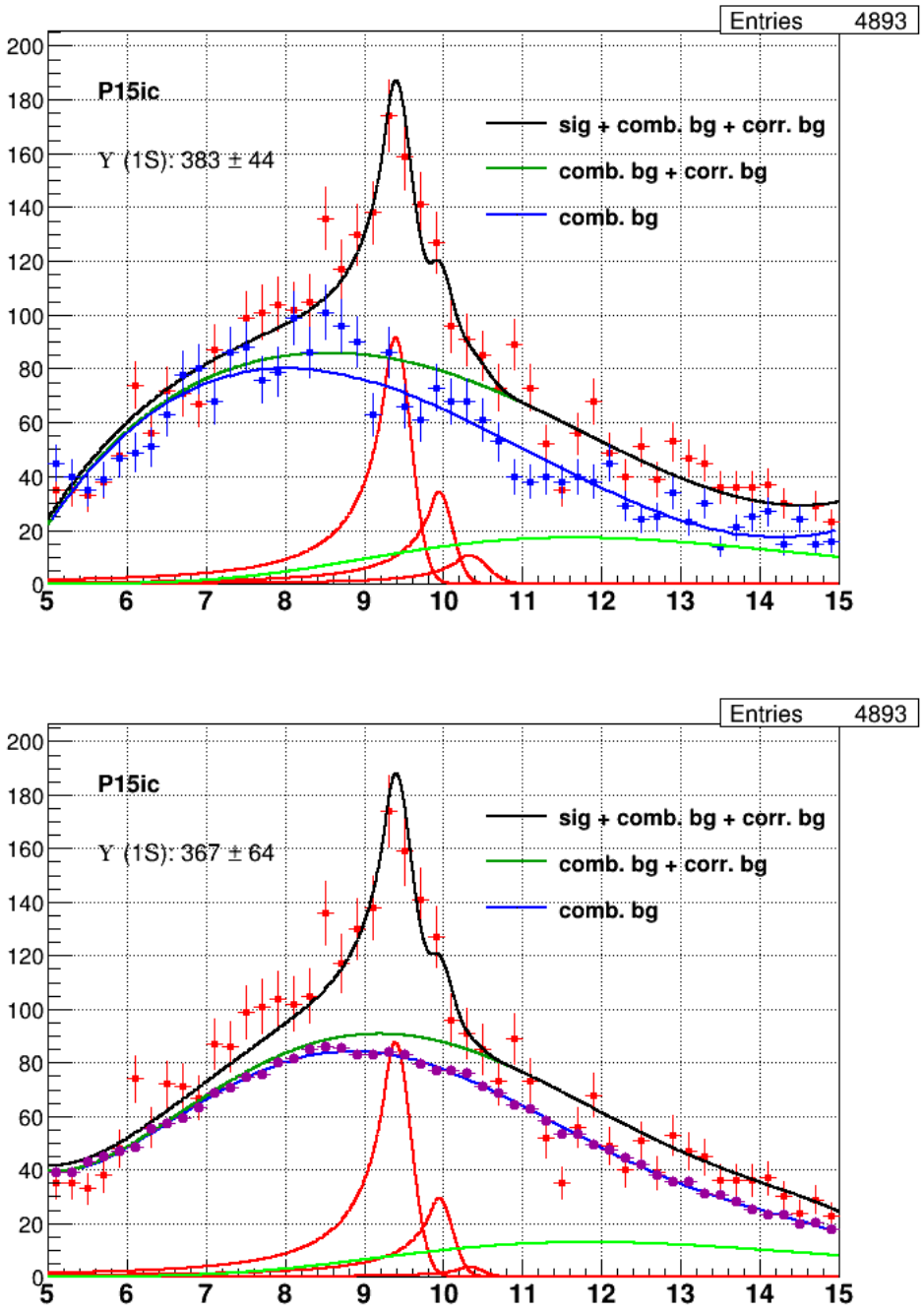

Fig. 3.12: This analysis: Di-electron invariant mass spectrum with the Υ signal. A composite fit including the signal peaks, the physical $B\bar{B}$ background, and the combinatorial background via like-signs (top) and event-mixing (bottom) is also plotted.

Summary and Outlooks

The objective of this work is to report the status of the author's analysis on Υ quarkonium production in heavy-ion collisions of $\sqrt{s_{\mathrm{NN}}} = 200$ GeV in the di-electron channel at the STAR experiment. In the first part, a brief introduction into the physics of heavy-ion collisions and the theory concerning heavy quarkonia is given. Subsequently, the experimental setup employed is overviewed in the second chapter. The third chapter, the principal part of this work, explains the author's research.

In the analysis, the di-electron invariant mass spectrum with a clear Υ(1S) and Υ(2S+3S) signal was reconstructed from high-tower–triggered Au+Au data from 2014. Used reconstruction methods and steps to determine reconstruction efficiencies are presented in great detail.

Furthermore, the Υ signals were carefully extracted. Expected signal shapes and contributions from physical background sources were obtained via Monte Carlo simulations. Both the like-sign and the event-mixing methods were employed to estimate the combinatorial background. The extracted yields can already bring valuable insight on the QGP properties, i.e. with a excited-to-ground state ratio.

The final objective of this analysis is to obtain the true Υ yields and present a R_{AA} for the ground and the excited states as a function of event activity and transverse momentum. Thus, in the future, a detailed analysis of the total reconstruction efficiency will be performed. The signal extraction methods will also be improved—the Drell-Yan background contribution will be evaluated and a better execution of the event-mixing method is also needed—to ensure a more stable fit with less uncertainties.

Bibliography

[1] ABELEV, B., et al. (ALICE Collaboration). Centrality determination of Pb-Pb collisions at $\sqrt{s_{\mathrm{NN}}}$=2.76 TeV with ALICE. *Physical Review C*. Vol. 88 (2013).

[2] MILLER, L., et al. Glauber Modeling in High Energy Nuclear Collisions. *Annual Review of Nuclear and Particle Science*. Vol. 57 (2007).

[3] SARKAR, S., et al. *The Physics of the Quark-Gluon Plasma A: Introductory Lectures.* Springer, c2010. ISBN 978-3-642-02286-9.

[4] MATSUI, T., SATZ., H. J/ψ Suppression by Quark-Gluon Plasma Formation. *Physical Letters B*. Vol. 178.

[5] EIDELMAN, S., et al. (Particle Data Group). Review of Particle Physics. *Physical Letters B*. Vol. 592.

[6] VOGT, R. *Ultrarelativistic Heavy-Ion Collisions.* Elsevier, 1st edition, c2007. ISBN 9780444521965.

[7] WONG, C. *Introduction to High-Energy Heavy Ion collisions*. Utopia Press, 1st edition, c1994. ISBN 978-981-02-0263-7 .

[8] TAWFIK, A., et al. Balance Function in High-Energy Collisions. *Advances in High Energy Physics*. Vol. 2015 (2015).

[9] MOCSY, A. Potential Models for Quarkonia. *European Physical Journal C*. Vol. 61 (2009).

[10] ADARE, A., et al. (PHENIX). Measurement of $\Upsilon(1S + 2S + 3S)$ production in $p + p$ and Au+Au collisions at $\sqrt{s_{\mathrm{NN}}} = 200$ GeV. *Physical Reviews C*. Vol. 91 (2014).

[11] EMERICK, A., et al. Bottomonia in the quark-gluon plasma and their production at RHIC and LHC. *European Physical Journal A*. Vol. 48 (2012).

[12] DAS, I. Upsilon production measurements in pp, p-Pb and Pb-Pb collisions with ALICE. *Quark Matter 2015* [online]. 2015. [ac. 15/09/17]. Available at: https://indico.cern.ch/event/355454/contributions/838966/ .

[13] LIN, Z., KO, C. Υ absorption in hadronic matter. *Physical Letters B*. Vol. 503 (2001).

[14] ANDERSON, M., et al. The Relativistic Heavy Ion Collider Project: RHIC and its Detectors. *Nuclear Instruments and Methods in Physics Research A*. Vol. 499 (2003).

[15] *Relativistic Heavy Ion Collider* [online]. Brookhaven National Laboratory. [ac. 01/09/17]. Available at: https://drupal.star.bnl.gov/STAR/public/img/SketchUpSTAR .

[16] ANDERSON, M., et al. The STAR Time Projection Chamber: A Unique Tool for Studying High Multiplicity Events at RHIC. *Nuclear Instruments and Methods in Physics Research A*. Vol. 499 (2003).

[17] BEDDO, M., et al. The STAR Barrel Electromagnetic Calorimeter. *Nuclear Instruments and Methods in Physics Research A*. Vol. 499 (2003).

[18] ALLISON, J., et al. Recent developments in GEANT4. *Nuclear Instruments and Methods in Physics Research A*. Vol. 835 (2016).

[19] SJOSTRAND, T., et al. A brief introduction to PYTHIA 8.1. *Computer Physics Communications*. Vol. 178 (2008).

[20] BAHR, M., et al. Herwig physics and manual. *European Physical Journal C*. Vol. 58 (2008).

PROCEEDINGS OF SCIENCE

Measurements of the Υ meson production in Au+Au collisions at the STAR experiment

Oliver Matonoha[*†]
Czech Technical University in Prague
E-mail: oliver.matonoha@fjfi.cvut.cz

In ultra-relativistic heavy-ion collisions, creation of a novel state of matter—a plasma of deconfined quarks and gluons—is expected. Quarkonium production is a crucial probe of this medium, since its suppression can be viewed as a direct evidence of the plasma formation. Moreover, it can be used to infer constraints on the medium temperature. In these proceedings, we present recent measurements on the Υ quarkonium production in Au+Au collisions at $\sqrt{s_{\mathrm{NN}}} = 200$ GeV via both the di-muon and di-electron channels by the STAR experiment at RHIC. At RHIC energies, secondary effects complicating the measured suppression are deemed less significant for the bottomonium family, which makes it a cleaner probe. The nuclear modification factor for the Υ states is reported and compared with similar measurements at the LHC as well as theoretical calculations. Moreover, the Υ production measurements in p+p and p+Au collisions are also presented. These provide a p+p reference with significantly improved precision and a quantification of the cold nuclear matter effect.

EPS-HEP 2017, European Physical Society conference on High Energy Physics
5-12 July 2017
Venice, Italy

[*]Speaker.
[†]On behalf of the STAR collaboration.

1. Introduction

Lattice QCD calculations predict that under extreme conditions, hadronic matter undergoes a phase transition and forms a plasma of deconfined quarks and gluons (QGP). This form of matter is hypothesised to comprise the universe in its earliest stages. Said conditions are believed to be present in ultra-relativistic heavy-ion collisions at the Relativistic Heavy Ion Collider (RHIC) and the Large Hadron Collider (LHC). Due to its short lifetime ($\sim$fm/c), the QGP is experimentally very challenging to measure.

One of the key probes of the QGP is the measurement of suppressed production of heavy quarkonia, e.g. J/ψ or Υ. The $c\bar{c}$ or $b\bar{b}$ pairs are created primarily before the QGP formation and their production cross-sections can be well calculated based on perturbative QCD. In the presence of the QGP, the quarkonium is expected to dissociate by *colour screening* when its radius exceeds the Debye radius $r_{\text{Debye}} \propto 1/T$ [1]. This dissociation is dependent on the quarkonium binding energy, and thus occurs for different states at different temperatures. Thanks to this *sequential melting* behaviour, quarkonia can serve as a "QGP thermometer" [2].

Other phenomena influence the quarkonium production in heavy-ion collisions, such as the *statistical recombination* by coalescence of deconfined quarks at the QGP phase boundary. There are also effects unrelated to the hot QGP phase—the *cold nuclear matter (CNM)* effects—like, for instance, the final state inelastic interactions with co-moving hadrons. The CNM effects can be investigated in p+A collisions. At RHIC energies, the Υ mesons are deemed a cleaner probe of the colour dissociation effect. This is mainly thanks to their lesser susceptibility to the co-mover absorption [3] and virtually no production by recombination, thanks to the b and $\bar{b}$ scarcity in the collisions [4].

2. Υ reconstruction with the STAR experiment

At the Solenoidal Tracker At RHIC experiment (STAR), Υ's are reconstructed via di-lepton decay channels in mid-rapidity. Time Projection Chamber (TPC) serves as the primary tracking sub-detector with full coverage in azimuth $0 < \varphi < 2\pi$ within pseudorapidity $|\eta| < 1$. It also provides PID for the leptons via measuring the energy loss $\mathrm{d}E/\mathrm{d}x$. For the di-electron channel, The Barrel Electromagnetic Calorimeter (BEMC) is employed. It has the same φ and η coverage as the TPC. Apart from electron PID via the E/p and the shower characteristics, it is also used for high-p_{T} electron triggering. Since 2014, STAR can also measure quarkonium production with the di-muon channel, thanks to the instalment of the Muon Telescope Detector (MTD), placed behind the solenoidal magnets. It covers approximately 45% in azimuth at $|\eta| < 0.5$ and is also used for muon triggering. By utilising both channels, weightier results on the quarkonium production are obtained.

3. Results

3.1 Υ production in p+p and p+Au collisions

Production of Υ(1S+2S+3S) has been measured via the di-electron channel in p+p collisions at $\sqrt{s} = 200$ GeV in BEMC–high-tower triggered data from 2015 of integrated luminosity 97 pb^{-1}.

Within $|y| < 0.5$, the p_{T}-integrated cross-section is $B \cdot \mathrm{d}\sigma/\mathrm{d}y = 81 \pm 5(\mathrm{stat.}) \pm 8(\mathrm{syst.})$ pb—see Fig. 1—where B is the di-electron decay branching ratio. This is consistent with STAR's previously published result [5] but is by a factor of two more precise. The result is also in solid agreement with world-wide experimental data trend as well as NLO CEM predictions [6].

Υ measurements have been carried out in p+Au collisions of $\sqrt{s_{\mathrm{NN}}} = 200$ GeV too, also using the di-electron channel and BEMC-triggered 2015 data with integrated luminosity 300 nb^{-1}. The measured nuclear modification factor is $R_{\mathrm{pAu}} = 0.82 \pm 0.10(\mathrm{stat.})^{-0.07}_{+0.08}(\mathrm{syst.}) \pm 0.10(\mathrm{norm.})$. The R_{pAu} is shown in Fig. 1 as a function of rapidity. These results seem to differ in trend compared to previous STAR results [5], however, they are still consistent within uncertainties.

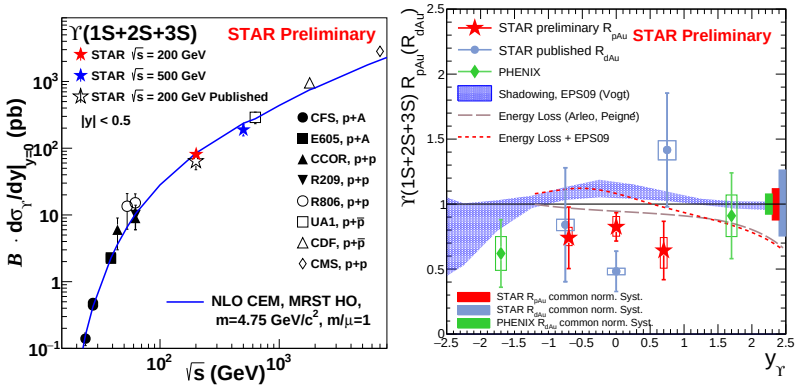

Figure 1: (*left*) Υ(1S+2S+3S) production cross-section at mid-rapidity from p+p collisions of $\sqrt{s} = 200$ GeV—displayed as a red star—compared with global results and NLO CEM calculations [6]; (*right*) Υ(1S+2S+3S) nuclear modification factor R_{pAu} from p+Au collisions of $\sqrt{s_{\mathrm{NN}}} = 200$ GeV—shown as red stars. Statistical, systematical, and global uncertainties are depicted as vertical bars, open boxes, and solid boxes respectively.

3.2 Υ production in Au+Au collisions

In Au+Au collisions of $\sqrt{s_{\mathrm{NN}}} = 200$ GeV, Υ production has been measured both in the di-electron channel (BEMC-triggered data from 2011 equivalent to 1.1 nb^{-1}) and the di-muon channel (MTD-triggered data from 2014 equivalent to 14 nb^{-1}). Nuclear modification factor R_{AA} results from both measurements are found to be consistent with each other within uncertainties and thus combined to further increase statistical precision.

The combined R_{AA} is reported in Fig. 2 as a function of mean number of participants N_{part} for both the Υ(1S) and the Υ(2S+3S). The excited states seem to be more suppressed in central collisions than the ground state. Shown are also results measured by CMS from Pb+Pb collisions of $\sqrt{s_{\mathrm{NN}}} = 2.76$ TeV [7]. Whereas the Υ(1S) results are well consistent, the Υ(2S+3S) appear to be less suppressed at RHIC than at LHC. The R_{AA} is also shown in Fig. 3 as a function of transverse momentum p_{T}. In comparison with the CMS results [7], the Υ(1S) is in solid agreement, whilst the Υ(2S+3S) seem to be less suppressed at high-p_{T}.

The results are compared to theoretical predictions in Fig. 4. Shown models for quarkonium production in heavy-ion collisions differ mainly in the implementation of various CNM effects and recombination as well as their approach towards the quarkonium binding potential. The Strongly

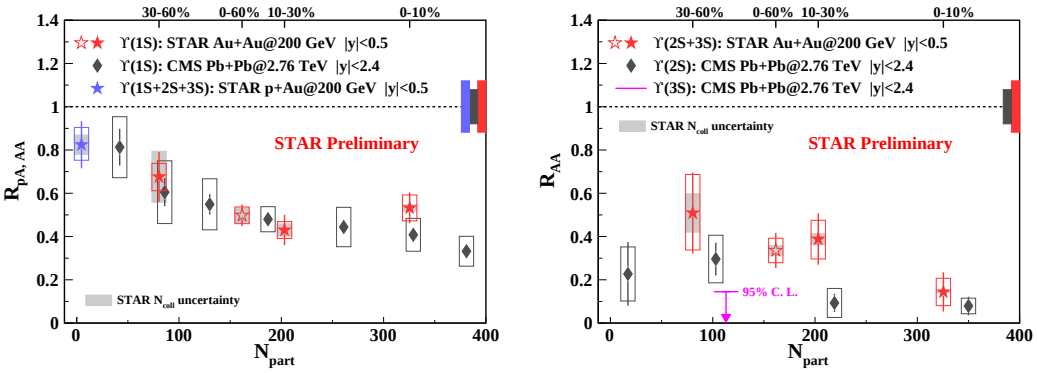

Figure 2: R_{AA} for the Υ(1S) (*left*) and the Υ(2S+3S) (*right*) in mid-rapidity shown as a function of N_{part} in Au+Au collisions of $\sqrt{s_{\mathrm{NN}}} = 200$ GeV—plotted as full red stars. Also portrayed is the centrality integrated result (open red star), the R_{pAu} from p+Au collisions (blue star), and CMS results from Pb+Pb collisions of $\sqrt{s_{\mathrm{NN}}} = 2.76$ TeV (grey diamonds and magenta line) [7]. Statistical and systematic uncertainties are shown as vertical bars and open boxes around the data points, shaded bands represent the systematic uncertainty from N_{coll}.

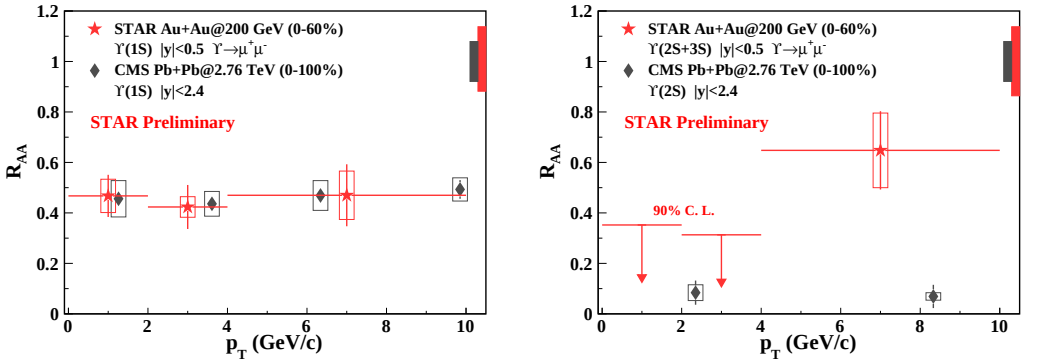

Figure 3: R_{AA} for the Υ(1S) (*left*) and the Υ(2S+3S) (*right*) in mid-rapidity shown as a function of p_{T} in Au+Au collisions of $\sqrt{s_{\mathrm{NN}}} = 200$ GeV—displayed as solid red stars. CMS results from Pb+Pb collisions of $\sqrt{s_{\mathrm{NN}}} = 2.76$ TeV are also shown (grey diamonds) [7]. Statistical and systematic uncertainties are depicted as vertical bars and open boxes around the data points, shaded bands represent the systematic uncertainty from N_{coll}.

Binding Scenario (SBS) models base the potential on the system internal energy. This corresponds to a fast Υ dissociation and neglects random thermal energy transfers with the medium, unlike the Weakly Binding Scenario (WBS). In the WBS, the potential is based on the system free energy. The Strickland-Bazow model [8] uses both of these approaches. The model by Liu, Chen, Xu, Zhang [9] includes dissociation only for the excited states and thus indicates the expected suppression caused by the feed-down solely. This model systematically under-predicts the suppression, hinting at further influence of CNM effects and/or direct Υ(1S) dissociation. Unlike the two previously mentioned models, the Emerick-Zhao-Rapp SBS model [4] takes into account CNM and regeneration effects. In summary, the data appear to favour the SBS models.

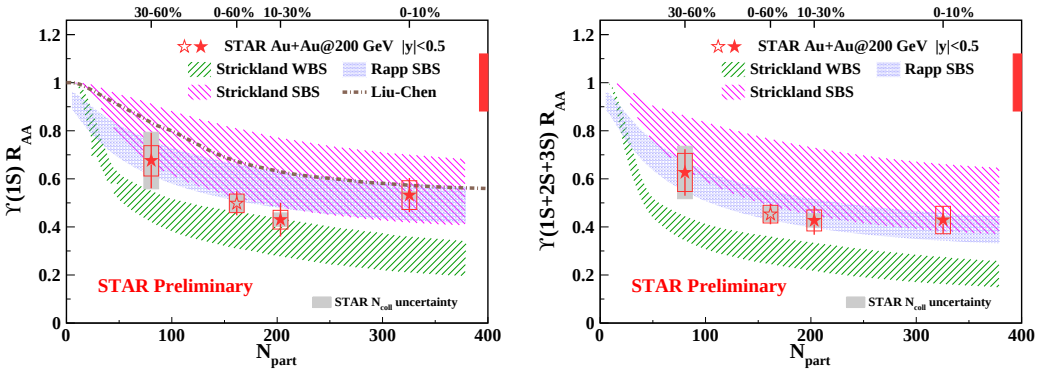

Figure 4: Nuclear modification factor R_{AA} for the Υ(1S) (*left*) and the Υ(1S+2S+3S) (*right*) from Au+Au collisions of $\sqrt{s_{\mathrm{NN}}} = 200$ GeV in mid-rapidity is shown as a function of mean number of participants N_{part}. Also shown are the predictions of following theoretical models: Strickland-Bazow (green and magenta area) [8], Emerick-Zhao-Rapp (blue area) [4], and Liu-Chen (grey line) [9].

4. Conclusions and Outlook

We present recent measurements on Υ measurements at mid-rapidity with the STAR experiment. In p+p collisions of $\sqrt{s} = 200$ GeV, the new and more precise cross-section results are in solid agreement with NLO CEM predictions as well as world-wide experimental data trend [6]. In p+Au collisions of $\sqrt{s_{\mathrm{NN}}} = 200$ GeV, the CNM effects are quantified via R_{pAu}. In Au+Au collisions, we present R_{AA} as a function of N_{part} and p_{T} for the Υ(1S) and the Υ(2S+3S). The Υ(1S) suppression at RHIC is similar to that at the LHC. Better understanding of CNM effects and the feed-down contribution is needed before drawing conclusions about direct Υ(1S) suppression. In the most central collisions, the Υ excited states are more suppressed than the ground state, which is in accordance with the sequential melting behaviour. The excited states also appear to be less suppresed at RHIC than at the LHC. These new Υ results can be further used to impose constraints on the QGP temperature at RHIC. Furthermore, analyses from other Au+Au data are underway, with increase in statistics by a factor of two.

References

[1] T. Matsui and H. Satz, Phys. Lett. B **178**, 416 (1986).

[2] A. Mocsy, Eu. Phys. Jour. C **61**, 705 (2009).

[3] Z. Lin and C. Ko, Phys. Lett. B **503**, 104 (2001).

[4] A. Emerick, X. Zhao, R. Rapp, Eu. Phys. Jour. A **48**, 72 (2012).

[5] The STAR collaboration, Phys. Lett. B **735**, 127 (2014).

[6] A. Frawley, T. Ullrich, R. Vogt, Phs. Rev. **462**, 125 (2008).

[7] The CMS collaboration, Phys. Lett. B **770**, 357 (2017).

[8] M. Strickland and D. Bazow, Nucl. Phys. A **879**, 25 (2012).

[9] Y. Liu, B. Chen, N. Xu, P. Zhuang, Phys. Lett. B **697**, 32 (2011).